

A New Partitioned 1D LTNE Continuum Model for the Simulation of 3D-Shaped Honeycomb Absorbers

Robin Tim Broeske^{a,*}, Peter Schwarzbözl^b, Bernhard Hoffschmidt^b

^a*DLR, Institute of Solar Research, Prof.-Rehm-Straße 1, 52428 Jülich, Germany*

^b*DLR, Institute of Solar Research, Linder Höhe, 51147 Köln, Germany*

Abstract

Porous absorber structures intended for open volumetric receivers of central tower power plants are receiving significant attention in current research. Due to the geometric complexity, volume-averaged continuum models are a common tool for the simulation of volumetric absorbers. Widely established for the investigation of ceramic foams, existing continuum models are less suitable for the simulation of honeycomb absorbers. 3D-shaped honeycomb absorber designs, i.e. absorbers with varying cross-sections, can pose additional challenges in the form of internal front-like surfaces, which are oriented perpendicular to the main channel axis. Due to the importance of the internal front-like surfaces w.r.t. absorption of solar radiation and convective heat transfer, a new partitioned 1D LTNE continuum model is proposed. The key innovation is the division of the absorber geometries into distinct sections forming a set of coupled LTNE models.

The new 1D continuum model has been successfully validated against a 3D CFD model. For nine compared simulation cases, the calculated thermal absorber efficiencies differ on average 0.81 percentage points between the two models. Simulations have been conducted for the state-of-the-art HiTRec absorber and two new absorber geometries. The StepRec absorber, a monolithic channel design with characteristic step-pins created via ceramic 3D screen printing out of SiSiC, reaches a thermal efficiency of up to 89.5 % for an air outlet temperature of 700 °C. A volumetric effect is predicted by for the new Emitec absorber, a channel geometry made of thin metal sheets, depending on the incident irradiation with efficiencies of up to 85.8 % at 700 °C.

Keywords: open volumetric receiver, CFD simulation, LTNE model

1. Introduction

As an alternative to the predominant molten salt or steam receivers, open volumetric receivers (OVR) for central receiver power plants using air as the heat transfer fluid have been the focus of extensive research. Improving the porous absorber structures of the OVR, crucial to the receiver efficiency and thus the yield of the power plant, has been one of the main goals. At the German Aerospace Center (DLR), research of the open volumetric receiver technology started in the mid nineties with an investigation of different ceramic absorber materials (Hoffschmidt et al., 2001). The pursuing research lead to the creation of the modular HiTRec ("High Temperature Receiver") technology with its ceramic honeycomb absorbers (Hoffschmidt et al., 2003). The upscaling of the technology (Hoffschmidt et al., 2001; Téllez et al., 2004) eventually resulted in the construction of the Solar Tower Jülich (Koll et al., 2009). The review by Ávila-Marín (2011) presents more extensive information on the development of the HiTRec technology and other types of open volumetric receivers. More recent research on porous absorbers for volumetric receivers focuses on 3D-shaped absorbers. The geometry and consequently the properties of these absorber vary along the flow direction which

can lead to improved thermal efficiencies. Multi-layer configurations of ceramic foams have been investigated by Roldán et al. (2014), Chen et al. (2015), and Zaversky et al. (2018). Ávila-Marín et al. (2014, 2018) conducted experiments on metal wire mesh absorbers with varying porosities, whereas Pabst et al. (2017) studied absorbers made of thin, stacked metal sheets. The honeycomb absorber¹ designs by Alberti et al. (2016) and Capuano et al. (2017) were made possible through additive manufacturing techniques. Alberti's hierarchical absorber was manufactured with the selective laser melting method, while electron beam melting was used to create an upscaled (3:1) version of the pin design by Capuano. Gomez-Garcia et al. (2015) proposed an absorber made of stacked layers of monolith channels, whereas Cagnoli et al. (2016) created an absorber geometry inspired by a compound parabolic concentrator. Many new 3D-shaped honeycomb absorber offer the potential of high thermal efficiencies, but cannot be readily modeled with standard continuum models due to internal front-like surfaces. Such surface areas are oriented perpendicular to the main channel axis and get reduced to points in one dimension by the volume-averaging approach. In this publication, a new partitioned 1D LTNE continuum model is introduced to addresses this chal-

*Corresponding author

Email address: robin.broeske@dlr.de (Robin Tim Broeske)

¹Within the context of this publication, honeycomb absorber refers to absorber structures characterized by parallel channels (opposed to e.g. porous foams).

Nomenclature

Acronyms

CFD	Computational Fluid Dynamics
DLR	German Aerospace Center
HiTRec	High Temperature Receiver
LTNE	local thermal non-equilibrium
OVR	Open Volumetric Receiver
SiSiC	siliconized silicon carbide

Greek Symbols

α	(= ε) absorptivity (-)
Δp	Pressure Loss (Pa)
ε	(= α) emissivity (-)
η	efficiency (-)
κ	heat conductivity ($\frac{W}{mK}$)
μ	dynamic viscosity (Pa s)
ρ	density ($\frac{kg}{m^3}$)
σ_{sb}	Stefan-Boltzmann constant ($\frac{W}{m^2 K^4}$)
Φ	porosity (-)
Ψ	viewfactor (-)

Roman Symbols

A	area (m^2)
A_{vol}	specific surface area ($\frac{m^2}{m^3}$)
C	coefficient (-)
c_p	specific heat capacity ($\frac{kJ}{kg K}$)
d	linear pressure coefficient ($\frac{1}{m^2}$)
E	mesh elements subset (-)
f	quadratic pressure coefficient ($\frac{1}{m}$)
G	irradiance ($\frac{W}{m^2}$)

h	convective heat transfer coefficient ($\frac{W}{m^2 K}$ resp. $\frac{W}{m^3 K}$)
I	incident irradiance ($\frac{W}{m^2}$)
J	surface radiosity ($\frac{W}{m^2}$)
L	length (m)
\dot{m}	massflow ($\frac{kg}{s}$)
$\frac{\dot{m}}{A}$	massflow density ($\frac{kg}{s m^2}$)
N	number/quantity (-)
n_1, n_2	coefficients (-)
Nu	Nusselt number (-)
op	opening angle (deg)
p	pressure (Pa)
\dot{Q}	heat flow (W)
\dot{q}	heat flux ($\frac{W}{m^2}$)
Re	Reynolds number (-)
T	temperature (K)
ti	tilt angle (deg)
U	velocity ($\frac{m}{s}$)
V	volume (m^3)
z	absorber depth (m)
\bar{z}	relative absorber depth (-)

Subscripts

1D	1D continuum model
3D	3D reference model
abs	absorber/absorbed
ap	aperture
blk	bulk
cr	cross-section
df	Darcy-Forchheimer
down	downstream

eff	effective
el	elements
emi	emission
f	fluid
fr	front
I	interface
i, j	section/interface index
in	inlet
k, l	viewfactor/radiation index
loss	loss
m, n	mesh element index
mat	material
mir	mirror
out	outlet
ph	physical
r	radiative
ref	reference
refl	reflection
s	solid
sec	section
sol	solar
tar	target
th	thermal
trans	transmission
u	unit cell index
uc	unit cell
up	upstream
vf	viewfactor
vol	volumetric
w	wall

lence and to allow for precise and fast simulations of new 3D-shaped absorbers. The new model is validated against the simulation results of a three-dimensional CFD model.

2. Volumetric Absorbers

The HiTRec absorber technology is used as the reference volumetric absorber for the conducted numerical simulations. The monolithic honeycomb absorber is made up of square channels with a channel width of 2 mm and a wall strength of 0.8 mm

(Hoffschmidt, 1997). The absorber matrix is manufactured by means of extrusion out of silicon carbide with a subsequent infiltration of additional silicon. The resulting siliconized silicon carbide (SiSiC) exhibits beneficial material properties for a volumetric absorber such as an surface absorptivity of 80 %, a high heat conductivity, and a high durability.

Two new absorber designs will be compared to the HiTRec absorber. The first new absorber called StepRec is based on a design originally proposed by Capuano et al. (2017). The smallest repeating element, also called the unit cell, for this design

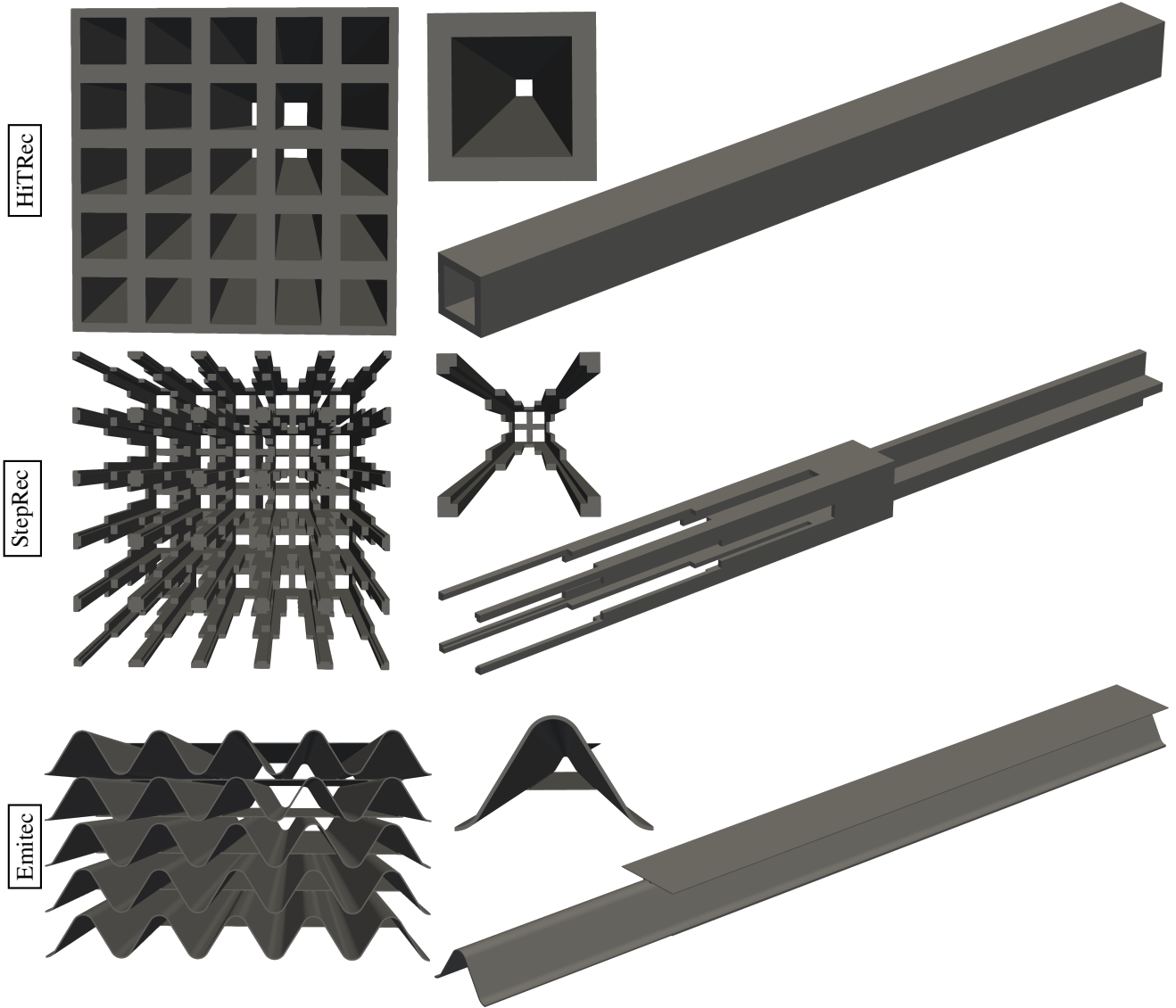


Figure 1: Unit cell models for the three absorber geometries. Left column shows a front view of 5 by 5 unit cells, right column a side and front view of a single unit cell, absorbers from top to bottom: HiTRec, StepRec, Emitec

consists of thin sloped pins at the irradiated absorber front followed by a square channel and a final shifted square channel. At the time, the 350 cpsi absorber proposed by Capuano could only be manufactured on a 3:1 scale (39 cpsi) out of an titanium aluminum alloy using electron beam melting (Capuano et al., 2017). The new StepRec absorber is instead fabricated by the company Exentis Technology GmbH using ceramic 3D screen printing. This technology allows for 87.5 cpsi absorbers (2:1 scale) to be build out of silicon carbide similar to the HiTRec absorber material. Likewise, the StepRec modules are also infiltrated with additional silicon. As a result, the HiTRec material properties are used for the simulations of the StepRec absorbers as similar properties are expected. One limitation of the 3D screen printing technology is that each change of the geometry in the printing direction requires a new screen. In particular, the continuously sloped pins of the design by Capuano would require constant screen changes making the geometry

impracticable and economically infeasible. The pins are therefore replaced with three steps of increasing width as shown in figure 1, giving the design its name. The curved section at the pin foundation is also removed.

The third absorber, the Emitec absorber, is a steel membrane absorber produced by the company Vitesco Technologies Emitec GmbH. The design is a continuation of metallic absorbers previously studied by Pabst et al. (2017). The absorber matrix is formed by alternating layers of curled and smooth layers of a high temperature steel alloy. Each steel sheet has a wall strength of only $65\text{ }\mu\text{m}$. Deviating from the previously studied absorbers, the smooth layers of the new design are shortened by 10 mm such that the front region of the absorber only contains curled steel sheets. This results in an increased porosity for the first absorber section. The channels formed by the alternating metal layers are characterized by a smooth and a sine-wave like side, where the orientation of the smooth side rotates be-

tween neighboring channels. Figure 1 shows one unit cell of the absorber centered on a channel with the smooth side at the bottom. The unit cell also contains two halves of upside-down channels. The steel alloy of the Emitec absorber exhibits a very high heat conductivity, but only a low surface absorptivity. Using a spectrometer, a surface absorptivity of 55 % was measured for a standard solar-weighted light spectrum. The metal probe was heated in an oven up to 800 °C before the measurement in order to account for darkening of the steel due to oxidation.

3. Modeling

Due to the geometric complexity of volumetric absorbers, fluid simulations of fully resolved absorber structures are generally too time-restrictive. As a result, numerical models for the simulation of porous absorber structures mostly follow two different approaches to bypass this restriction. Single channel (unit cell models) use conventional 3D fluid simulations, however the simulated geometry is strongly reduced (sec. 3.6). Contrary, continuum models do not explicitly resolve the absorber geometries, but instead rely on volume-averaged temperature fields and effective parameters. These parameters include among others the porosity (void volume fraction of the total absorber volume) or the specific surface area per total volume. The majority of the existing continuum models relies on the Local Thermal Non-Equilibrium (LTNE) approach opposed to the simpler Local Thermal Equilibrium concept (Ávila-Marín et al., 2019). LTNE modeling entails two temperature fields for the fluid phase and the solid absorber with separate differential equations. The two phases are coupled via convective heat transfer. For one-dimensional continuum models, the only coordinate represents the main flow direction, which corresponds to the main channel axis for honeycomb absorbers. LTNE models have also been applied in two and three dimensions, e.g. in connection with non-homogeneous boundary conditions (cf. Ávila-Marín et al., 2019). Radiation modeling varies significantly between existing continuum models. Common are radiation models based on the radiative transfer equation (Modest, 2013). These range from the simple Rosseland's approximation (e.g. Sano et al., 2012) and P1 model (e.g. Wu et al., 2011) to the more complex and more time-intensive discrete ordinate method (e.g. Pitz-Paal et al., 1997). Models based on raytracing algorithms are also used, e.g. as a reference for simpler radiation models (Kribus et al., 2014). An extensive overview of all published continuum models is given in the review by Ávila-Marín et al. (2019).

The newly presented model is a 1D continuum model with local thermal non-equilibrium (LTNE). The central innovation of the new model is the explicit division of the absorber geometries into specific absorber sections. The model has been implemented within the framework of the open-source software OpenFOAM® (2021). The 3D CFD model used for the validation of the new continuum model is introduced in section 3.6.

3.1. Absorber Sections and Interfaces

The StepRec absorber and the Emitec absorber present new challenges for the continuum modeling in the form of internal

front-like surfaces. These surfaces, like the absorber front, are oriented perpendicular to the main flow direction and get reduced to single points in one dimension. Such discontinuities within the simulated absorber volume cannot be accurately depicted with standard 1D LTNE models. However, the internal front-like surfaces, which include the step front surfaces for the StepRec geometry and the front area of the retracted smooth steel layers for the Emitec absorber, play an important role for the absorption of the solar radiation and the convective heat transfer between the two phases. The new model solves the problem of the internal front-like surfaces through the division of the absorber geometries into distinct absorber sections and interfaces. Figure 2 shows the five absorber sections of the StepRec geometry. The absorber is separated at each transition between the steps, the transition from the third step to the base channel, and the transition between the base channel and the shifted channel. Each of the sections is modeled as an individual volume with temperature fields for the solid and the fluid phase. The volumetric equations (sec. 3.2) are solved for each section separately. The sections are connected through boundary conditions for the absorber interfaces (eq. 20 - 23). Each absorber interface represents the plane between two neighboring sections containing the internal front-like surfaces. Additionally, local, dimension-less coordinate systems \bar{z}_j are defined for each section. These coordinate systems are oriented along the main flow direction and are connected to the global coordinate system z through the section lengths L_j :

$$\begin{cases} d\bar{z}_j = \frac{1}{L_j} dz \\ \bar{z}_j = 0 \Leftrightarrow z = \sum_{i=0}^{j-1} L_i \\ \bar{z}_j = 1 \Leftrightarrow z = \sum_{i=0}^j L_i \end{cases} \quad (1)$$

As the continuum model is intended to be used as part of a design process for new absorber geometries, the relative local coordinate systems will allow the section lengths to be adjusted as part of the optimization process without changes to the numerical grid. In figure 3, the surface areas of the different interfaces for the StepRec geometry are highlighted. Not visible is the downstream surface area of interface number 3, which is the only two-sided interface with an upstream and a downstream facing surface area for the studied volumetric absorbers. Opposite to the five sections of the StepRec geometry, the Emitec absorber consists of only two sections and one interface. The first 10 mm of the absorber, from which the smooth metal sheets were retracted, comprise the initial section, while the other 30 mm represent the second section. The front area of the retracted layers make up the surface of the only interface. The HiTRec absorber has only one section and no interface. The sections lengths, porosity values, and specific surface areas are listed in table 1 for each section of the three absorber geometries.

3.2. Governing Equations

For the fluid temperature $T_{f,j}$ and the solid temperature $T_{s,j}$, differential equations 2 and 3 are defined similar to existing continuum models (e.g. Kribus et al., 2014). However, the

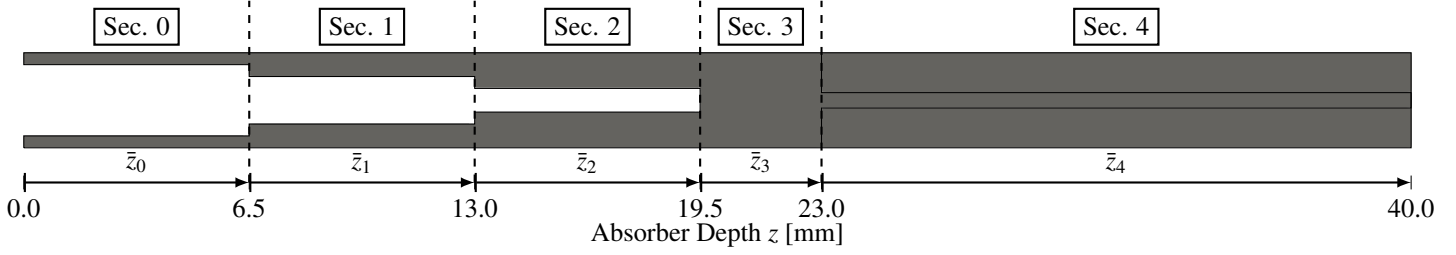


Figure 2: Absorber sections and local coordinate systems for the StepRec geometry

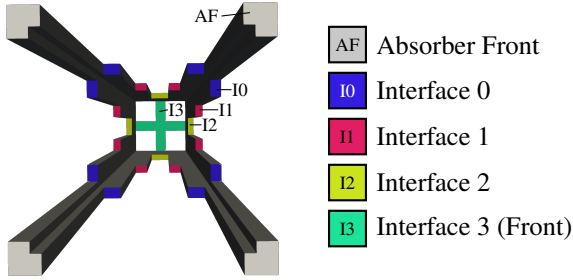


Figure 3: Interface surface areas for the StepRec geometry. Not visible is the downstream facing surface area of interface no. 3.

Table 1: Key geometric parameters for the three absorber geometries

Absorber	Section j	Length L_j [mm]	Porosity Φ_j [-]	Specific Surface Area $A_{vol,j}$ [m^2/m^3]
HiTRec	0	40	51.0 %	1020
	1	6.5	94.5 %	366.7
StepRec	2	6.5	86.5 %	733.3
	3	3.5	70.3 %	1230
	4	17	70.3 %	1230
	5	17	70.3 %	1230
Emitec	0	10	94.9 %	1581
	1	30	91.3 %	2333

equations are solved for each absorber section within the respective local coordinate systems. The two phases are connected through convective heat transfer represented by the volumetric heat transfer coefficients $h_{vol,j}$. The local coefficients are updated throughout the simulations from Nusselt correlations for each section (app. A.2). Heat conduction within both phases is considered, while the solid temperature equation also includes the radiation source term $\frac{d\dot{q}_{r,j}}{d\bar{z}_j}$. This source term is calculated by the radiation models described in section 3.3. The porosity of the absorber sections is denoted by Φ_j (cf. table 1).

$$\frac{1}{L_j} \frac{d}{d\bar{z}_j} \left(\frac{\dot{m}}{A} c_p T_{f,j}(\bar{z}_j) \right) = \frac{1}{L_j^2} \frac{d}{d\bar{z}_j} \left(\Phi_j \kappa_f \frac{dT_{f,j}}{d\bar{z}_j} \right) + h_{vol,j} (T_{s,j}(\bar{z}_j) - T_{f,j}(\bar{z}_j)) \quad (2)$$

$$0 = \frac{1}{L_j^2} \frac{d}{d\bar{z}_j} \left((1 - \Phi_j) \kappa_s \frac{dT_{s,j}}{d\bar{z}_j} \right) - h_{vol,j} (T_{s,j}(\bar{z}_j) - T_{f,j}(\bar{z}_j)) - \frac{d\dot{q}_{r,j}}{d\bar{z}_j} \quad (3)$$

The continuum equation in one dimension (eq. 4) leads to a constant massflow density $\frac{\dot{m}}{A}$ for the entire absorber volume. For the conducted simulations, the unit cell cross-section of each absorber (solid + void) is used as the reference area A to allow for a better comparison of the continuum model to the reference 3D model (sec. 3.6).

$$\frac{1}{L_j} \frac{d}{d\bar{z}_j} (\rho U_{ph,j}) = 0 \quad (4)$$

$$\frac{1}{L_j} \frac{dp_j}{d\bar{z}_j} = \mu d_{df,j} U_{df,j}(\bar{z}_j) + \rho \frac{f_{df,j}}{2} U_{df,j}^2(\bar{z}_j) \quad (5)$$

Equation 5 represents the Darcy-Forchheimer equation describing the pressure gradient within a porous medium (Becker et al., 2006). The Darcy velocity $U_{df,j}$ is connected to the physical flow velocity $U_{ph,j}$ through the porosity: $U_{df,j} = \Phi_j U_{ph,j}$. The geometry-dependent Darcy-Forchheimer coefficients $d_{df,j}$ and $f_{df,j}$ are determined numerically (app. A.3). By combining equations 4 and 5, a second order differential equation for the air pressure p_j is created. The derivation of the pressure equation is based on Soullaine (2016), where the same approach was applied to the linear Darcy equation.

$$0 = -\frac{1}{L_j^2} \frac{d}{d\bar{z}_j} \left(\frac{1}{\Phi_j} \frac{\rho}{d_{df,j} \mu + \frac{f_{df,j}}{2} \frac{\dot{m}}{A}} \frac{dp_j}{d\bar{z}_j} \right) \quad (6)$$

Air properties are calculated using the local air temperature and pressure. The property models are based on data from Stephan et al. (2013). Using the local densities values, the local flow velocities can be derived from the massflow density: $U_{df,j} = \frac{1}{\rho(T_{f,j})} \frac{\dot{m}}{A}$. For the SiSiC absorber material, experimental data from the German Aerospace Center is used for the heat conductivity. Data for the heat conductivity of the Emitec steel alloy was provided by the manufacturer.

3.3. Radiation Modeling

For the radiative transport, separate approaches are implemented for the solar irradiation and the thermal radiation emitted by the absorber surfaces. The volumetric, radiative source

term for the temperature equation of the solid phase (eq. 3) is defined as the sum of the contributions by the solar irradiation and the thermal radiation:

$$\frac{d\dot{q}_{r,j}}{d\bar{z}_j} = \frac{d\dot{q}_{r,sol,j}}{d\bar{z}_j} + \frac{d\dot{q}_{r,th,j}}{d\bar{z}_j} \quad (7)$$

Solar Irradiation

The absorption of solar irradiation by the absorber surface is calculated using the raytraycer FEMRay². The raytracing results in a three-dimensional flux distribution for the absorbed solar radiation within the porous absorbers. From this distribution, a one-dimensional function $C_{sol,vol,j}(\bar{z}_j)$ is derived for each section, such that the volumetrically absorbed solar power is given by:

$$-\frac{d\dot{q}_{r,sol,j}}{d\bar{z}_j} = \frac{I_{ap}}{L_{abs}} C_{sol,vol,j}(\bar{z}_j) \quad (8)$$

The functions $C_{sol,vol,j}$ are defined relative to the total absorber depth L_{abs} and the aperture normal irradiance I_{ap} , where the absorber aperture is the plane containing the absorber front surface. Besides the absorber geometry, the distribution functions also depend on the absorptivity α_{mat} of the absorber material and the direction of the incident solar irradiation (cf. table 2). However, the magnitude of the irradiance has no influence and the same functions can therefore be used for multiple simulations with varying flux levels. Equation 8 is evaluated once at the start of each simulation and the solar irradiation only interacts with the model for the thermal radiation through the temperature equation of the solid phase.

Thermal Radiation

A surface-to-surface radiation model based on (effective) viewfactors is used to model thermal radiation within the absorbers. The single viewfactor model used for this purpose must encompass all N_{sec} absorber sections, all $N_{sec} - 1$ interfaces, and the absorber inlet and outlet. Unfortunately, the numerical tool which is used to calculate the viewfactors does not support periodic geometries, which would be well suited to model absorber geometries with partly open channels and radiative exchange among neighboring channels. To bypass this restriction, the viewfactors are determined for an array of N_{uc} connected unit cells (e.g. a 3-by-3 pattern) for the StepRec and Emitec geometry. To limit the required array size, the radiation volume is closed at the sides with N_{mir} mirror elements to replace the open channel sides of the outermost unit cells.

For the radiation model, an additional discretization of each absorber section into segments is created along the main channel axis. All surface areas of the absorber channel located within one segment are combined, and are treated as a single surface by the radiation model. Overall, $N_{vol,el}$ of these artificial surfaces, called volume radiation elements, are created for the absorber sections. The discretization of each section is chosen

based on the 3D surface mesh used for the viewfactor calculation (cf. app. A.5) and is in general not equal to the total number of 1D elements used for the continuum model (cf. table 4). The forwards and backwards facing interface surface areas are also combined and treated as single surfaces, the interface radiation elements, for each absorber interface. The absorber front is not part of the radiation model as it has no radiative exchange with the absorber inside (cf. eq. 14). Instead, the void area of the absorber aperture, i.e. the plane containing the absorber front, is combined to form the inlet radiation element for each unit cell. Outlet radiation elements are created in a similar fashion for the absorber exit. All radiation elements are assigned effective viewfactors $\Psi_{k,l}^{eff}$, the calculation of which is explained in appendix A.5.

In total, the thermal radiation model consists of $N_{el,vf} = N_{uc}(N_{el,vol} + N_{sec} + 1) + N_{mir}$ viewfactor elements. For each element k , the net radiative (surface) flux $\dot{q}_{r,k}$ is defined as the difference of the irradiance G_k and surface radiosity J_k :

$$\dot{q}_{r,k} = G_k - J_k \quad (9)$$

The surface radiosity is the sum of surface emission and reflected irradiance. In turn, the irradiance depends on the surface radiosities of all other elements and the effective viewfactors $\Psi_{k,l}^{eff}$ between the elements:

$$J_k = \varepsilon_k \sigma_{sb} T_k^4 + (1 - \varepsilon_k) G_k, \quad (10)$$

$$G_k = \sum_{l=0}^{N_{el,vf}-1} \Psi_{k,l}^{eff} J_l \quad (11)$$

For each of the $N_{el,vol}$ volume radiation elements, the temperature T_k is interpolated from the solid temperature $T_{s,j}$ of the corresponding 1D elements, while the emissivity ε_k is set to the material emissivity ε_{mat} . Similarly, the interface temperatures $T_{s,I,j}$ (eq. 20) and the material emissivity are used for the $N_{sec} - 1$ interface radiation elements. The temperature distribution is assumed to be identical for all absorber unit cells of the simulated pattern. The temperature profile is thus copied onto the (volume & interface) elements representing the remaining $N_{uc} - 1$ unit cells. The copied elements also receive the material emissivity.

All N_{uc} inlet elements are modeled as black surfaces ($\varepsilon_k = 1$) with a temperature of zero Kelvin. Incoming thermal radiation from the surroundings is neglected. Additionally, radiation exchange with the area behind the absorber is also neglected assuming this area's temperature is close to the temperature level at the absorber outlet. The N_{uc} outlet elements and the N_{mir} mirror elements are set as perfect reflectors ($\varepsilon_k = 0$) with artificial temperatures. These artificial temperatures are updated throughout the simulation based on the irradiance to yield a local net radiative flux of zero:

$$T_{out/mir,k} = \sqrt[4]{\frac{G_{out/mir,k}}{\sigma_{sb}}} \quad (12)$$

Equations 9 - 11 combine to form a system of linear equations, which is solved as part of the continuum model. The irradiance G_j^{eff} and net radiative flux $\dot{q}_{r,j}^{eff}$ are interpolated for each

²FEMRay is the in-house name for an extension of the raytracing software MIRVAL. This extension, which was developed at the DLR, allows the use of finite element meshes with MIRVAL (cf. Amsbeck et al., 2008; Schwarzbözl et al., 2008).

1D mesh element from the volume radiation elements. Finally, the volumetric source term for equation 7 is defined as follows, where $A_{vol,j}$ is the specific surface area of absorber section j (cf. table 1):

$$\frac{d\dot{q}_{r,th,j}}{d\bar{z}_j} = \varepsilon_{mat} A_{vol,j} (\sigma_{sb} T_{s,j}^4 (\bar{z}_j) - G_j^{eff}) \quad (13)$$

3.4. Boundary Conditions

The model requires $2N_{sec}$ boundary conditions for each of the three volumetric equations, one for the beginning and the end of each section. The boundary conditions can be categorized as boundary conditions for the absorber front, the absorber outlet, and the $N_{sec} - 1$ interfaces.

Absorber Front

The boundary conditions for the absorber front are applied to the start of the first section ($\bar{z}_0 = 0$), which coincides with the global origin ($z = 0$). The area in front of the absorber is not part of the modeled volume, but the convective heat transfer in this region is accounted for by the inlet boundary conditions. For the solid absorber front surface, the energy balance given by equation 14 links the convection with absorption of the solar irradiation, radiation emitted by the front, and heat conduction to the solid bulk absorber.

$$0 = \alpha_{mat} I_{ap} - \varepsilon_{mat} \sigma_{sb} T_{s,0}^4(0) + \kappa_s \frac{1}{L_0} \frac{dT_{s,0}}{d\bar{z}_0} \Big|_{\bar{z}_0=0} - h_{fr} (T_{s,0}(0) - T_{f,0}(0)) \quad (14)$$

The convective heat transfer coefficient h_{fr} is updated during each solver iteration from a Nusselt number correlation (app. A.2). The convective heat is absorbed by the air flow before it enters the absorber leading to the boundary condition given by equation 15. The temperature of the air reaching the absorber T_{in} is a constant input, while the porosity of the absorber front is assumed to be equal to the bulk porosity of the first absorber section (Φ_0). Heat conduction within the air flow is also accounted for.

$$\frac{\dot{m}}{A} c_p (T_{f,0}(0) - T_{in}) = (1 - \Phi_0) h_{fr} (T_{s,0}(0) - T_{f,0}(0)) + \Phi_0 \kappa_f \frac{1}{L_0} \frac{dT_{f,0}}{d\bar{z}_0} \Big|_{\bar{z}_0=0} \quad (15)$$

The boundary condition for the pressure equation models the pressure loss caused by the absorber inlet based on the Darcy-Forchheimer equation (eq. 5). The coefficients $d_{df,fr}$ and $f_{df,fr}$ are evaluated together with the Darcy-Forchheimer coefficients for the volume equation (app. A.3). The total absorber length $L_{abs} = \sum_{j=0}^{N_{sec}-1} L_j$ is used as the reference length and the reference pressure is set to $p_{in} = 1$ bar.

$$p_0(0) = p_{in} - L_{abs} \left(d_{df,fr} \mu + \frac{f_{df,fr}}{2} \frac{\dot{m}}{A} \right) U_{df,0}(0) \quad (16)$$

Absorber Outlet

The absorber exit is located at the end of the last section ($\bar{z}_{N_{sec}-1} = 1$) and it is assumed that no energy is exchanged with the area behind the absorber. Therefore, the gradients of both temperature fields are set to zero at the outlet:

$$\frac{1}{L_{N_{sec}-1}} \frac{dT_{s,N_{sec}-1}}{d\bar{z}_{N_{sec}-1}} \Big|_{\bar{z}_{N_{sec}-1}=1} = 0 \quad (17)$$

$$\frac{1}{L_{N_{sec}-1}} \frac{dT_{f,N_{sec}-1}}{d\bar{z}_{N_{sec}-1}} \Big|_{\bar{z}_{N_{sec}-1}=1} = 0 \quad (18)$$

The pressure gradient at the absorber exit is set according to the Darcy-Forchheimer equation using the coefficients of the last section. Similar to the pressure differential equation, this pressure boundary condition was derived from a boundary condition by Soullaine (2016).

$$\frac{1}{L_{N_{sec}-1}} \frac{dp_{N_{sec}-1}}{d\bar{z}_{N_{sec}-1}} \Big|_{\bar{z}_{N_{sec}-1}=1} = \left(d_{df,N_{sec}-1} \mu + \frac{f_{df,N_{sec}-1}}{2} \frac{\dot{m}}{A} \right) U_{df,N_{sec}-1}(1) \quad (19)$$

Interfaces

The boundary conditions for the $N_{sec} - 1$ interfaces serve two purposes. They connect the volumetric absorber sections in a pair-wise manner, but also allow the internal front-like surfaces to be modeled more precisely through the energy balance given by equation 20. Each interface j is defined through the porosity of the upstream section Φ_j , the porosity of the downstream section Φ_{j+1} , and the porosity of the interface itself $\Phi_{I,j}$. For the given absorber geometries, only the fourth interface of the StepRec geometry between the normal and the shifted channel sections is two-sided. All other interfaces are one-sided and have only an upstream facing front-like surface. For these interfaces, the interface porosity is equal to the porosity of the downstream section, and the interface boundary conditions simplify accordingly. The interface energy balance connects heat conduction in the solid phase with convective heat transfer at the internal front-like surfaces, thermal radiation exchange, and direct solar irradiation:

$$0 = - (1 - \Phi_j) \kappa_s \frac{1}{L_j} \frac{dT_{s,j}}{d\bar{z}_j} \Big|_{\bar{z}_j=1} + (1 - \Phi_{j+1}) \kappa_s \frac{1}{L_{j+1}} \frac{dT_{s,j+1}}{d\bar{z}_{j+1}} \Big|_{\bar{z}_{j+1}=0} - (\Phi_j - \Phi_{I,j}) h_{I,up,j} (T_{s,I,j} - T_{f,I,j}) - (\Phi_{j+1} - \Phi_{I,j}) h_{I,down,j} (T_{s,I,j} - T_{f,I,j}) - (\Phi_j + \Phi_{j+1} - 2\Phi_{I,j}) \varepsilon_{mat} \sigma_{sb} T_{s,I,j}^4 + \alpha_{mat} G_{I,j} + I_{ap} C_{sol,I,j} \quad (20)$$

The thermal irradiance of the interface $G_{I,j}$ is calculated as part of the viewfactor model, while the coefficient $C_{sol,I,j}$ describes a possible direct solar irradiation of the interface relative to

the power incident in the absorber aperture (eq. 26). The energy balance is solved for the solid interface temperature $T_{s,I,j}$, which is also applied as the boundary value for the corresponding sections:

$$T_{s,j}(1) = T_{s,j+1}(0) = T_{s,I,j} \quad (21)$$

The convective heat transfer coefficients for each interface are determined together with the volumetric heat transfer coefficients (app. A.2). The interface fluid temperature $T_{f,I,j}$ is defined as the fluid temperature in the interface cross-section, where the convective heat flow across the forwards facing front-like surface has been absorbed by the air flow, but the heat flow across the downstream face has not yet been absorbed. As heat conduction in the air flow is considered (eq. 2), the conductive heat flow across interfaces has to be continuous. Combined, the following three equations can be derived which are solved for the temperatures $T_{f,I,j}$, $T_{f,j}(1)$, and $T_{f,j+1}(0)$. The heat transfer coefficients are also repeatedly updated as they depend on the fluid and solid interface temperatures.

$$\begin{cases} \Phi_j K_f \frac{1}{L_j} \frac{dT_{f,j}}{dz_j} \Big|_{\bar{z}_j=1} = \Phi_{j+1} K_f \frac{1}{L_{j+1}} \frac{dT_{f,j+1}}{dz_{j+1}} \Big|_{\bar{z}_{j+1}=0} \\ \frac{\dot{m}}{A} c_p (T_{f,I,j} - T_{f,j}(1)) = (\Phi_j - \Phi_{I,j}) h_{I,up,j} (T_{s,I,j} - T_{f,I,j}) \\ \frac{\dot{m}}{A} c_p (T_{f,j+1}(0) - T_{f,I,j}) = (\Phi_{j+1} - \Phi_{I,j}) h_{I,down,j} (T_{s,I,j} - T_{f,I,j}) \end{cases} \quad (22)$$

To link the pressure differential equations across the interfaces, the pressure gradient on the upstream side is set based on the Darcy-Forchheimer equation similar to the absorber exit boundary condition (eq. 19). For the downstream side, a pressure jump is prescribed analogous to the absorber front boundary condition (eq. 16). The coefficients of the upstream section are used to calculate the gradient, while the pressure jump is described by interface-specific coefficients (app. A.3).

$$\begin{cases} \frac{1}{L_j} \frac{dp_j}{dz_j} \Big|_{\bar{z}_j=1} = \left(d_{df,j} \mu + \frac{f_{df,j}}{2} \frac{\dot{m}}{A} \right) U_j(1) \\ p_{j+1}(0) = p_j(1) - L_{abs} \left(d_{df,I,j} \mu + \frac{f_{df,I,j}}{2} \frac{\dot{m}}{A} \right) U_{j+1}(0) \end{cases} \quad (23)$$

3.5. Performance Evaluation

The presented model allows for a detailed analysis of the absorber performance as each of the different loss mechanisms can be quantified separately. For the absorber front, the absorbed solar radiation $\dot{Q}_{abs,fr}$ and the reflection losses $\dot{Q}_{loss,refl,fr}$ are directly defined by the front porosity and material absorptivity. Both are proportional to the total incoming radiation \dot{Q}_{ap} :

$$\dot{Q}_{abs,fr} = A I_{ap} (1 - \Phi_0) \alpha_{mat} \quad (24)$$

$$\dot{Q}_{loss,refl,fr} = A I_{ap} (1 - \Phi_0) (1 - \alpha_{mat}) \quad (25)$$

$$\dot{Q}_{ap} = A I_{ap} \quad (26)$$

The reflection losses from the bulk absorber $\dot{Q}_{loss,refl,blk}$, the power absorbed within the absorber $\dot{Q}_{abs,blk}$, and the transmission losses $\dot{Q}_{loss,trans}$ are calculated as part of the raytracing simulations. The emission losses for the absorber front $\dot{Q}_{loss,emi,fr}$ and the bulk absorber $\dot{Q}_{loss,emi,blk}$ are given through the front

temperature and the integral of the net radiative flux over the absorber sections:

$$\dot{Q}_{ss,emi,fr} = A \varepsilon_{mat} \sigma_{sb} T_{s,0}^4(0) \quad (27)$$

$$\dot{Q}_{loss,emi,blk} = A \sum_{j=0}^{N_{sec}} L_j A_{vol,j} \int_0^1 \dot{q}_{r,j}^{eff}(\bar{z}_j) d\bar{z}_j \quad (28)$$

Comparing the loss mechanisms to the total incoming solar irradiation leads to the absorber efficiency:

$$\eta_{th} = 1 - \frac{1}{\dot{Q}_{ap}} \left(\dot{Q}_{loss,refl,fr} + \dot{Q}_{loss,refl,blk} + \dot{Q}_{loss,trans} + \dot{Q}_{loss,emi,fr} + \dot{Q}_{loss,emi,blk} \right) \quad (29)$$

3.6. Reference 3D-Model

To validate the new continuum model, a three-dimensional CFD model is employed. The simulated geometries are restricted to representative parts of the absorber geometries ("unit cells", cf. fig. 1) in order to limit the required computational effort. This is a common approach ("detail simulation", cf. Ávila-Marín et al., 2019) for the simulation of volumetric absorbers and exemplarily has been applied by Kopanidis et al. (2010), Fend et al. (2013), and Cagnoli et al. (2016). It is assumed that the result of the small geometry can be extrapolated to the overall absorber matrix. The CFD model combines the simulation of the air flow through the absorber with solving heat conduction within the absorber material. The air flow is modeled based on the stationary, laminar, compressible Navier-Stokes equations neglecting buoyancy forces. Similar to the continuum model, the absorption of the solar irradiation is determined via raytracing, while the thermal radiation is represented through a surface-to-surface viewfactor radiation model. The same restrictions regarding the calculation of periodic viewfactors, which apply for the continuum model (cf. sec. 3.3, app. A.5), also apply for the 3D model. The radiative exchange within the 3D model is therefore similarly solved for a 3-by-3 pattern of absorber unit cells with copied temperature distributions, while the flow field is only calculated for the original unit cell. The different parts of the model are connected through an energy balance which is solved for each mesh element on the absorber surface. As for the continuum model, the 3D reference model is implemented within the software OpenFOAM®(2021).

4. Results

Three sets of simulations have been carried out for the three absorber geometries using the new continuum model and the reference 3D-model. Each simulation case is defined through the aperture (normal) irradiance I_{ap} , a tilt angle ti , an opening angle op , the inlet temperature T_{in} , and the target for the air outlet temperature T_{tar} . The values for these properties are given in table 2 for each simulation case. For the studied geometries, the absorber aperture is defined as the plane which contains the absorber front. The raytracing simulations calculating the absorption of the solar irradiation start at the absorber apertures,

Table 2: Defining properties of the three simulation cases

Case	$I_{ap} [\frac{kW}{m^2}]$	$ti [deg.]$	$op [deg.]$	$T_{in} [^{\circ}C]$	$T_{tar} [^{\circ}C]$
A	1000	0.0	15	100	700
B	1000	30	15	100	700
C	485.0	30	15	100	700

i.e. the initial starting positions of the rays are generated uniformly distributed across the free channel cross-sections within the apertures. The initial direction of the incoming radiation is controlled through the tilt angle and the opening angle. The tilt angle describes the vertical deviation of the average ray direction from the main channel axis. A tilt angle of zero corresponds to an average direction parallel to the channel axis, whereas a positive value means the irradiation has an initial upwards direction. Based on the given opening angle, the direction of each ray is randomly disturbed such that all simulated directions form a cone around the average direction with the radius defined by the opening angle. The used raytracing software also supports a third angle allowing for lateral rotation, this option however was not activated for the simulations. The irradiation direction of the simulation cases B and C are intended to approximate the irradiation of a volumetric receiver at the top of a tower system from a heliostat field. Simulation case A is meant to model the irradiation distribution of a high-flux solar simulation such as German Aerospace Center’s Synlight (Wieghardt et al., 2018). The used aperture irradiances and air temperature values are based on typical values for the receiver of the Solar Tower Juelich, while the air inlet temperature of 100 °C has been chosen to account for an air return system (cf. Stadler et al., 2019).

To achieve the target air outlet temperature, the massflow density $\frac{\dot{m}}{A}$ was iteratively adjusted during the simulations with the new continuum model. The resulting densities are specified in table 3. For the 3D reference model, the massflow densities were held constant at the values calculated with the continuum model.

Table 3: Massflow densities for three simulation cases

Case	Massflow Density $\frac{\dot{m}}{A} [\frac{kg}{s \cdot m^2}]$		
	HiTRec	StepRec	Emitec
A	1.211	1.343	1.329
B	1.211	1.337	1.224
C	0.5790	0.6720	0.5910

4.1. Mesh Independence

The computational grids for the continuum model consist of simple line elements discretizing the absorber depth along the main channel axis. To show the mesh independence of the simulation results, three different grid levels ranging from 250 to 1000 elements were generated for each absorber geometry. The mesh elements were distributed evenly between the different absorber sections for each grid. Table 4 compares the thermal

efficiency for simulation case A for all three geometries and mesh levels. The efficiencies change less than one tenth of a percentage point clearly showing the mesh independence. For the StepRec geometry, an increased number of mesh elements was necessary to yield a stable simulation for the coarsest grid level. The three-dimensional reference model requires compu-

Table 4: Results of the mesh independence study for the 1D continuum model

Mesh Level	HiTRec		StepRec		Emitec	
	No. El.	th. Eff. [-]	No. El.	th. Eff. [-]	No. El.	th. Eff. [-]
Coarse	250	78.2 %	375	86.7 %	250	85.8 %
Medium	500	78.2 %	500	86.7 %	500	85.8 %
Fine	1000	78.2 %	1000	86.7 %	1000	85.8 %

tational grids for the solid volume of the absorber unit cell and for the void volume including the inlet area. Numerical meshes containing mostly hexahedron elements have been used. Table 5 lists the results of a mesh independence study for the 3D model, which was conducted in the same manner as for the continuum model. Three levels with increasing number of elements were used, the total number of elements per level for both volume meshes is listed in the table. As for the continuum model, the thermal efficiencies show no significant dependence on the used mesh. While the coarse mesh levels are sufficient w.r.t calculation of the thermal efficiency, the medium mesh levels were used for all further simulations for both models as this improved the resolution of the temperature distributions (cf. fig. 7).

Table 5: Results of the mesh independence study for the 3D reference model

Mesh Level	HiTRec		StepRec		Emitec	
	No. El.	th. Eff. [-]	No. El.	th. Eff. [-]	No. El.	th. Eff. [-]
Coarse	0.21 mio	77.4 %	0.48 mio	85.4 %	0.60 mio	85.7 %
Medium	1.2 mio	77.5 %	2.4 mio	85.5 %	3.1 mio	85.7 %
Fine	7.2 mio	77.5 %	15 mio	85.4 %	16 mio	85.7 %

4.2. Irradiation Results

Figure 4 shows the results of the raytracing simulations relative to the total incoming radiation. As the same raytracing software is used for the continuum model and the reference 3D model, the irradiation results do not differ between both models and only one result is shown per geometry. Simulation cases B and C only vary with respect to the aperture irradiance I_{ap} , but not regarding the direction of the incoming radiation. The results relative to \dot{Q}_{ap} are therefore identical for the two cases and are shown together as the lower plot in figure 4. The StepRec geometry absorbs marginally less than eighty-nine percent of the incoming solar radiation for simulation case A, while the Emitec and HiTRec absorbers collect only 87.4 % resp. 85.2 % of the incident power. A significant part of the irradiation is transmitted through all three structures for case A, but none is transmitted for the tilted irradiation of cases B and C. Instead, the power reflected out of the bulk absorbers is increased for all geometries for cases B and C, most significantly for the Emitec absorber. The total absorbed power is also increased for all geometries compared to case A, the increase ranging from 0.7 % for Emitec to 7.4 % for StepRec. Corresponding to the front

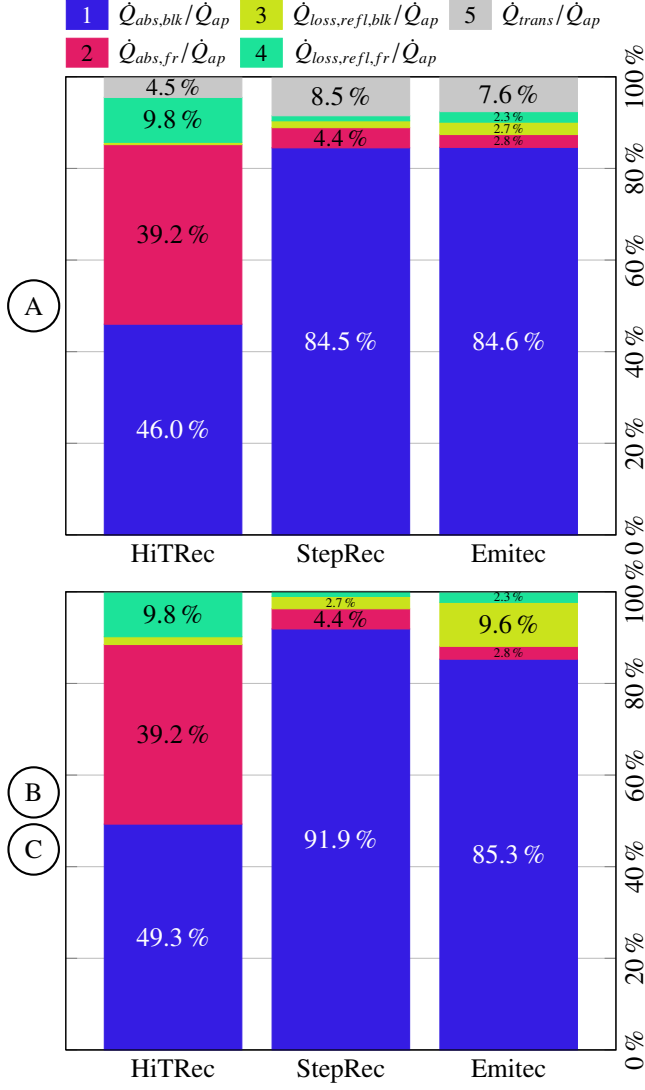


Figure 4: Absorbed solar irradiation and optical losses relative to the total incoming radiation for the three simulation cases (legend numbers represent the category order from bottom (1) to top (5))

porosities, the absorbed irradiation is divided almost evenly between the absorber front and absorber bulk for the HiTRec geometry, whereas only small fractions of the light are absorbed by the front of StepRec and Emitec.

4.3. Thermal Efficiency Results

The simulation results for the continuum model and the reference 3D model are presented in figures 5 and 7. Figure 5 compares the calculated thermal efficiencies against the different loss mechanisms. The reflection and transmission losses are summarized as the optical losses $\dot{Q}_{loss,opt}$. For each simulation case and each geometry, the 1D and 3D results are shown next to each other.

The identical absorber ordering with respect to the thermal efficiency is predicted by both models. The StepRec absorber reaches the best thermal efficiency for all three simulation cases, while the HiTRec absorber ranks last for all three cases.

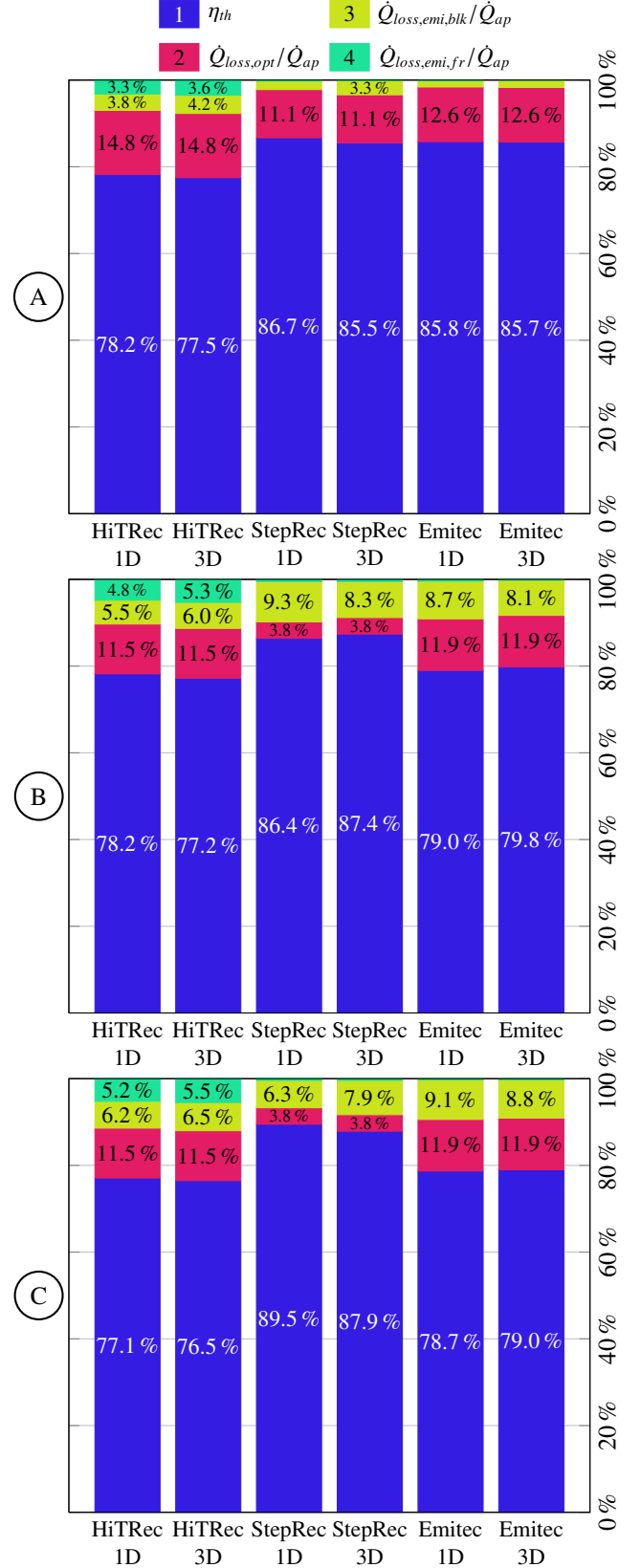


Figure 5: Integral simulation results for both models for all simulation cases and geometries (legend numbers represent the category order from bottom (1) to top (4))

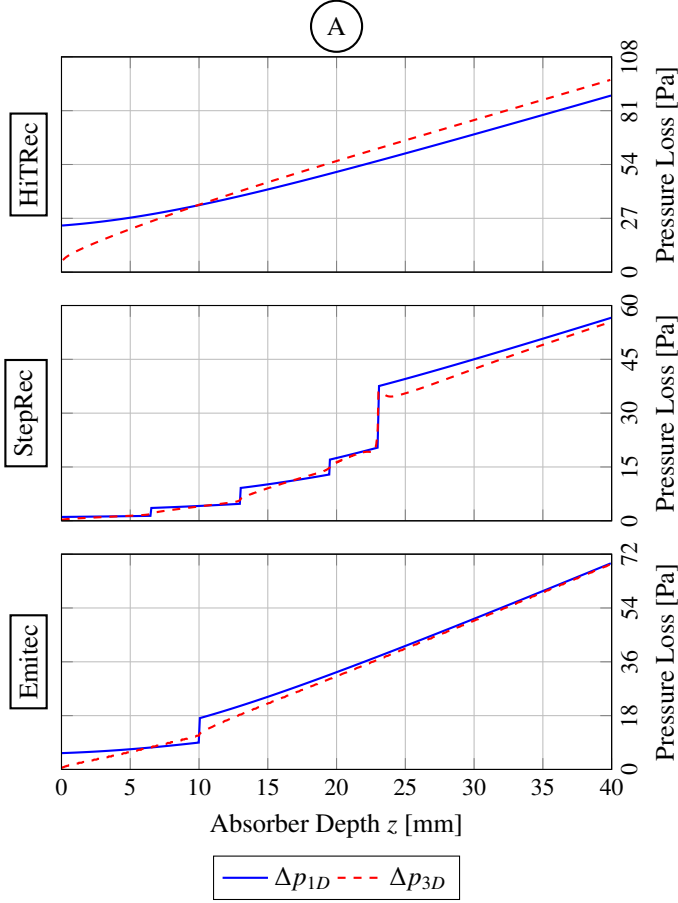


Figure 6: Pressure loss distribution over absorber depth for simulation case A for the three absorbers. The local pressure loss is defined as $\Delta p_j(\bar{z}_j) = p_{in} - p_j(\bar{z}_j)$

The Emitec geometry matches the efficiency level of StepRec for case A, but performs significantly worse than StepRec for cases B and C, closer to the level of HiTRec. On average, the continuum model results differ by 0.81 percentage points from the reference 3D model. The best match is found for the Emitec absorber for case A with a separation of less than one tenth of a percentage point, the largest difference of 1.6 percentage points occurs for case C for the StepRec geometry. The optical losses are identical for both models because they are calculated using the same raytracing software. As a result, the efficiency differences directly correspond to differences in the calculated emission losses. For StepRec and Emitec, emission losses from the absorber front are negligible, whereas the emission losses are close to evenly split between front and bulk for HiTRec. The thermal efficiency of the Emitec absorber drops significantly from case A to case B with the changed irradiation direction, while it remains on the same levels for the other two geometries. With the decreasing flux density from 1 MW (case B) to 485 kW (case C), only the efficiency of the StepRec absorber increases with small reductions for HiTRec and Emitec. The temperature profiles for the solid and the fluid phase are plotted over the absorber depth in figure 7. Each subplot com-

pare the results of the continuum model against the reference 3D model for one simulation case for one absorber. In case of the 3D model, massflow-weighted average values are shown for the fluid temperature and volume-weighted averages for the solid temperature. Overall, the continuum model matches the results of the reference model well. The agreement between both models is particularly good for the zones of thermal equilibrium at the end of the absorbers. The outlet temperatures ($T_{f,N_{sec}-1}(1)$) differ only by 5.8 K on average. Larger discrepancies can be found within the absorber entry regions, most visible for simulation case B. The continuum model predicts a 104 K higher solid front temperature ($T_{s,0}(0)$) for the Emitec absorber for case B, whereas the average difference for the remaining simulations is only 21 K.

A significant volumetric effect is shown for the Emitec geometry for simulation case A. The solid front temperature is calculated to be more than 200 K below the air outlet temperature. The StepRec absorber also exhibits a volumetric effect of around 40 K for case A, while no volumetric effect can be found for any geometry for case B and for all cases for the HiTRec absorber. Emitec and StepRec are both close to a volumetric effect for case C, as the front temperature exceeds the air outlet temperature less than ten degrees. The Emitec geometry shows the largest zone of (approximate) thermal equilibrium between the two phases for all three cases. The most important parameters for achieving the volumetric effect are a high convective heat transfer and a deep penetration of the incoming solar radiation. Due to its large specific surface area (cf. table 1), the Emitec absorber has significantly higher volumetric convective heat transfer coefficients compared to the other two designs (cf. fig. A.1). The open design of StepRec absorber in turn allows for the deepest penetration of the solar radiation (cf. fig. A.3 + A.4). The HiTRec geometry absorbs a substantial amount the incoming radiation at the absorber front because of its low front porosity. Combined with insufficient convective heat transfer, the HiTRec absorber fails to achieve the volumetric effect. The inclination of the solar radiation for simulation cases B and C (cf. table 2) leads to a lower penetration depth for all geometries compared to case A. As a consequence, the strongest volumetric effects can be found for case A. The lower aperture irradiance of case C enables the new designs to almost reach the volumetric effect despite the inclined irradiation direction in contrast to case B.

As part of the new continuum model, the pressure within the porous absorber structures is solved based on equation 6. Figure 6 compares the pressure distribution over the absorber depth for simulation case A for the three absorber geometries. The reference 3D model results are shown in addition to the 1D model results. A good agreement between both models can be observed. Compared to the 3D model, the continuum models underestimates the total pressure loss by 8.0 Pa for HiTRec and overestimates it by 1.7 Pa resp. 0.3 Pa for StepRec and Emitec. For all three simulation cases, the average difference between the two models is 2.4 Pa. Pressure jumps caused by changes in the geometric absorber cross-sections (at the location of internal front-like surfaces) are depicted accurately by the 1D model.

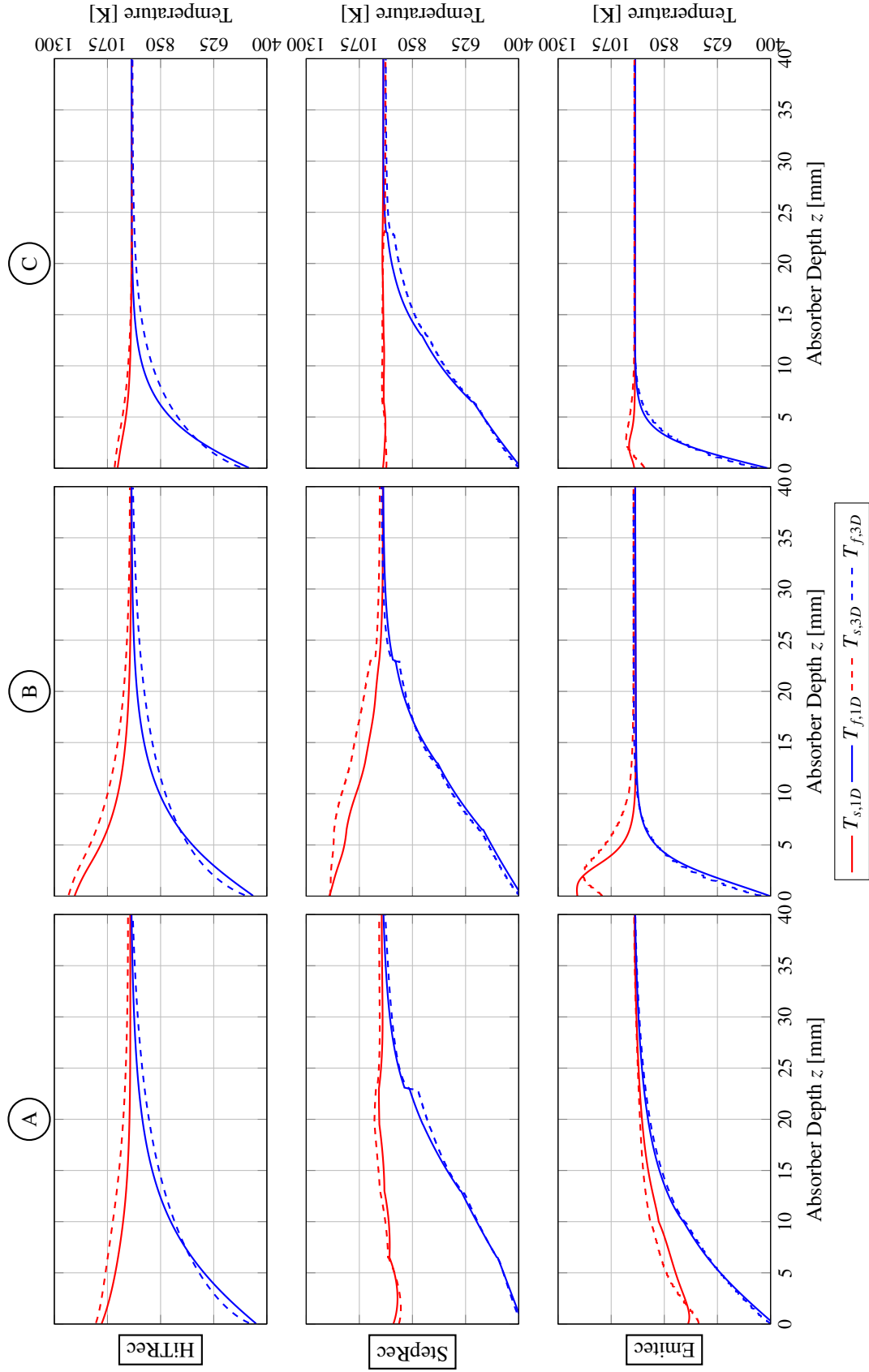


Figure 7: Temperature distribution over absorber depth for both models for all simulation cases and geometries: Each column shows the results for one simulation case, each row the results for one absorber geometry.

5. Discussion

The continuum model results show a reasonable agreement with the reference 3D model. The largest differences in the calculated temperature distributions occurred towards the absorber fronts. Within the entry region of a volumetric absorber, the flow is not fully hydraulically and thermally developed. Additionally, the largest (air) temperature gradients are located within this region. The volume-averaging approach of the continuum model can be therefore expected to affect the entry region more strongly than the zone of thermal equilibrium towards the absorber exit. The integral results for the thermal absorber efficiencies showed an average difference of 0.81 percentage points between the two models. For five out of nine conducted simulations, the continuum models predicts a higher efficiency and a lower efficiency is calculated for three simulations with one exact match. Thus, no indication of a systematic deviation in the continuum model could be found. The new continuum model can therefore be deemed as accurate as the reference 3D model. Auxiliary simulations calculating the different effective parameters are needed for the continuum model. However, these simulations require significantly less numerical effort compared to the flow simulation of the 3D reference model. As a result, the continuum model is faster than the 3D model even for a single simulation case. For each absorber, their pressure loss coefficients, Nusselt correlations and viewfactors could be reused for the three investigated simulation cases. Only two different raytracing simulations had to be conducted per absorber geometry, further increasing the speed advantage of the 1D model. As the new model is intended to be used as part of an optimization process, which typically require the evaluation of numerous geometry variants, the speed advantage of the new model will therefore become necessary in order to keep the calculation time of such a process within feasible limits.

6. Conclusion and Outlook

A new local one-dimension thermal non-equilibrium model for the simulation of volumetric absorbers has been developed. The central new approach of the model is the division of the absorber geometries into specific absorber sections and solving the overall problem as a set of coupled LTNE models. In particular, this allows for a very detailed representation of internal front-like surfaces, surfaces which are perpendicular to the main flow direction and reduce to a single point in one dimension. Further important aspects of the model include separate treatment of solar and thermal radiation, a viewfactor based model for the thermal radiation, and the partial differential equation based on the Darcy-Forchheimer equation for the pressure within the absorber. The continuum model has been successfully applied to simulate two new absorber geometries, the StepRec absorber and the Emitec absorber, and the reference HiTRec absorber. The validation against the reference three-dimension CFD model showed a very good agreement regarding the thermal absorber efficiencies and the temperature profiles across the ab-

sorber depth. Based on the new continuum model, a design/optimization process for new 3D-shaped absorber structures is being developed. Experimental tests at the Solar Tower Juelich and the Synlight are also planned for the two new promising absorber designs StepRec and Emitec. These test results will further be used to continue the validation of the new continuum model.

Acknowledgements

This work was supported by the German Federal Ministry for Economic Affairs and Energy on the basis of a decision by the German Bundestag, reference number 0324300B.

References

- Alberti, F., Santiago, S., Roccabruna, M., Luque, S., Gonzalez-Aguilar, J., Crema, L., Romero, M., 2016. Numerical analysis of radiation propagation in innovative volumetric receivers based on selective laser melting techniques, in: AIP Conference Proceedings, p. 030001. doi:10.1063/1.4949053.
- Amsbeck, L., Buck, R., Heller, P., Jedamski, J., Uhlig, R., 2008. Development of a tube receiver for a solar-hybrid microturbine system, in: 14th Biennial CSP Solarpaces Symposium 2008.
- Ávila-Marín, A., Fernández-Reche, J., Martínez-Tarifa, A., 2019. Modelling strategies for porous structures as solar receivers in central receiver systems: A review. *Renewable and Sustainable Energy Reviews* 111, 15–33. doi:10.1016/j.rser.2019.03.059.
- Ávila-Marín, A.L., 2011. Volumetric receivers in solar thermal power plants with central receiver system technology: A review. *Solar Energy* 85, 891–910. doi:10.1016/j.solener.2011.02.002.
- Ávila-Marín, A.L., Alvarez-Lara, M., Fernández-Reche, J., 2014. Experimental results of gradual porosity wire mesh absorber for volumetric receivers. *Energy Procedia* 49, 275–283. doi:10.1016/j.egypro.2014.03.030.
- Ávila-Marín, A.L., Alvarez de Lara, M., Fernández-Reche, J., 2018. Experimental results of gradual porosity volumetric air receivers with wire meshes. *Renewable Energy* 122, 339–353. doi:10.1016/j.renene.2018.01.073.
- Becker, M., Fend, T., Hoffschmidt, B., Pitz-Paal, R., Reutter, O., Stamatov, V., Steven, M., Trimis, D., 2006. Theoretical and numerical investigation of flow stability in porous materials applied as volumetric solar receivers. *Solar Energy* 80, 1241–1248. doi:10.1016/j.solener.2005.11.006.
- Cagnoli, M., Savoldi, L., Zanino, R., Zaversky, F., 2016. Numerical evaluation of an innovative cup layout for open volumetric solar air receivers. AIP Conference Proceedings 1734, 030007. doi:10.1063/1.4949059.
- Capuano, R., Fend, T., Stadler, H., Hoffschmidt, B., Pitz-Paal, R., 2017. Optimized volumetric solar receiver: Thermal performance prediction and experimental validation. *Renewable Energy* 114, 556–566. doi:10.1016/j.renene.2017.07.071.
- Chen, X., Xia, X.L., Meng, X.L., Dong, X.H., 2015. Thermal performance analysis on a volumetric solar receiver with double-layer ceramic foam. *Energy Conversion and Management* 97, 282–289. doi:10.1016/j.enconman.2015.03.066.
- Fend, T., Schwarzbözl, P., Smirnova, O., Schöllgen, D., Jakob, C., 2013. Numerical investigation of flow and heat transfer in a volumetric solar receiver. *Renewable Energy* 60, 655–661. doi:10.1016/j.renene.2013.06.001.
- Gomez-Garcia, F., Gonzalez-Aguilar, J., Tamayo-Pacheco, S., Olalde, G., Romero, M., 2015. Numerical analysis of radiation propagation in a multi-layer volumetric solar absorber composed of a stack of square grids. *Solar Energy* 121, 94–102. doi:10.1016/j.solener.2015.04.047.
- Hoffschmidt, B., 1997. Vergleichende Bewertung verschiedener Konzepte volumetrischer Strahlungsempfänger. Dissertation. DLR.
- Hoffschmidt, B., Fernandez, F., Hennecke, K., Romero, M., Stobbe, P., Téllez, F., 2001. Development of ceramic volumetric receiver technology, in: 5th Cologne Solar Symposium, Cologne, 21.06.01.
- Hoffschmidt, B., Téllez, F.M., Valverde, A., Fernández, J., Fernández, V., 2003. Performance evaluation of the 200-kWth HiTRec-II open volumetric air receiver. *Journal of Solar Energy Engineering* 125, 87–94. doi:10.1115/1.1530627.

Koll, G., Schwarzbözl, P., Hennecke, K., Hartz, T., Schmitz, M., Hoffschmidt, B., 2009. The solar tower jülich - a research and demonstration plant for central receiver systems, in: Proceedings of the 15th SolarPACES Conference.

Kopanidis, A., Theodorakakos, A., Gavaises, E., Bouris, D., 2010. 3d numerical simulation of flow and conjugate heat transfer through a pore scale model of high porosity open cell metal foam. International Journal of Heat and Mass Transfer 53, 2539–2550. doi:10.1016/j.ijheatmasstransfer.2009.12.067.

Kribus, A., Gray, Y., Grijnevich, M., Mittelman, G., Mey-Cloutier, S., Caliot, C., 2014. The promise and challenge of solar volumetric absorbers. Solar Energy 110, 463–481. doi:10.1016/j.solener.2014.09.035.

Modest, M.F., 2013. Radiative heat transfer. Academic press. doi:10.1016/C2010-0-65874-3.

Pabst, C., Feckler, G., Schmitz, S., Smirnova, O., Capuano, R., Hirth, P., Fend, T., 2017. Experimental performance of an advanced metal volumetric air receiver for solar towers. Renewable Energy 106, 91–98. doi:10.1016/j.renene.2017.01.016.

Pitz-Paal, R., Hoffschmidt, B., Böhmer, M., Becker, M., 1997. Experimental and numerical evaluation of performance and flow stability of different types of open volumetric absorbers under non-homogeneous irradiation. Solar Energy 60, 135–150. doi:10.1016/S0038-092X(97)00007-8.

Roldán, M.I., Smirnova, O., Fend, T., Casas, J.L., Zarza, E., 2014. Thermal analysis and design of a volumetric solar absorber depending on the porosity. Renewable Energy 62, 116–128. doi:10.1016/j.renene.2013.06.043.

Sano, Y., Iwase, S., Nakayama, A., 2012. A local thermal nonequilibrium analysis of silicon carbide ceramic foam as a solar volumetric receiver. Journal of Solar Energy Engineering 134, 021006. doi:10.1115/1.4005758.

Schwarzbözl, P., Belhomme, B., Buck, R., Uhlig, R., Amsbeck, L., Schmitz, M., 2008. Simulation solarer Turmsysteme, in: 11. Kölner Sonnenkolloquium.

Soulaine, C., 2016. Introduction to computational fluid mechanics using the openfoam® technology. <https://documents.pub/document/introduction-to-computational-fluid-mechanics-using-the-web-csoulainoftrainingopenfoamintroduction.html>. Accessed: 15.03.2019.

Stadler, H., Maldonado, D., Offergeld, M., Schwarzbözl, P., Trautner, J., 2019. Cfd model for the performance estimation of open volumetric receivers and comparison with experimental data. Solar Energy 177, 634–641. doi:10.1016/j.solener.2018.11.068.

Stephan, P., Kabelac, S., Kind, M., Martin, H., Mewes, D., Schaber, K. (Eds.), 2013. VDI-Wärmeatlas. Springer Berlin Heidelberg. doi:10.1007/978-3-642-19981-3.

Téllez, F., Romero, M., Heller, P., Valverde, A., Dibowski, G., Ulmer, S., 2004. Thermal performance of solair 3000 kwh ceramic volumetric solar receiver, in: Ramos, C., Huacuz, J. (Eds.), 12th International Symposium Solar Power and Chemical Energy Systems, October 6 - 8, 2004, Oaxaca, Mexico, Instituto de Investigaciones Electricas.

The OpenFOAM Foundation, 2021. Openfoam — free cfd software — the openfoam foundation. <https://openfoam.org/>. Accessed: 14.07.2021.

Wiegardt, K., Laaber, D., Dohmen, V., Hilger, P., Korber, D., Funken, K.H., Hoffschmidt, B., 2018. Synlight - a new facility for large-scale testing in csp and solar chemistry, in: Proceedings of the 23rd SolarPACES Conference. doi:10.1063/1.5067078.

Wu, Z., Caliot, C., Flamant, G., Wang, Z., 2011. Coupled radiation and flow modeling in ceramic foam volumetric solar air receivers. Solar Energy 85, 2374–2385. doi:10.1016/j.solener.2011.06.030.

Zaversky, F., Aldaz, L., Sánchez, M., Ávila-Marín, A.L., Roldán, M.I., Fernández-Reche, J., Füssel, A., Beckert, W., Adler, J., 2018. Numerical and experimental evaluation and optimization of ceramic foam as solar absorber – single-layer vs multi-layer configurations. Applied Energy 210, 351–375. doi:10.1016/j.apenergy.2017.11.003.

Appendix A. Correlations for Effective Parameters

The continuum model relies on various so called effective parameters for the simulation of the volumetric absorbers which have to be calculated before the simulations.

A.1. Geometric Parameters

The first group of effective parameters describes the absorber geometries structurally, these parameters include the length L_j , the porosity Φ_j , and the specific surface area $A_{vol,j}$ of each absorber section. For the investigated absorber geometries, the structure parameters have constant values per absorber section and were calculated analytically as given in table 1.

A.2. Nusselt Numbers

A central component of the continuum model is the convective heat exchange between the fluid and solid phase. In the volumetric differential equations 2 and 3, the exchange is depicted through a volumetric convective heat transfer coefficient $h_{vol,j}$. Additionally, convective heat transfer is also part of the boundary conditions for the absorber front (eq. 14 - 15) and the absorber interfaces (eq. 20 - 22). Each coefficient required by these equations is updated throughout the simulations of the continuum model based on Nusselt number correlations. These Nusselt number correlations are derived numerically before the main simulations. Three-dimensional, stationary, laminar and compressible fluid simulations are carried out for the absorber unit cells with added empty inlet areas. The absorber wall temperature is set to a constant value for the whole geometry. For each mesh element on the absorber surface, the local heat flow is calculated using a local surface-normal temperature gradient and the local heat conductivity. Integrating over and dividing by the corresponding surface areas yields the average convective heat flux for each section (\dot{q}_j) and for each interface ($\dot{q}_{I,j}$). For two-sided interfaces (e.g. fourth interface of the StepRec absorber) $\dot{q}_{I,j}$ is divided into the heat flux across the forward-facing ($\dot{q}_{I,up,j}$) and backward-face ($\dot{q}_{I,down,j}$) surface areas. Reference temperatures $T_{ref,j}$ are defined for each section based on a massflow-volume average over all mesh elements m of the section volume V_j :

$$T_{ref,j} = \frac{\sum_{m \in V_j} \dot{m}_m V_m T_m}{\sum_{m \in V_j} \dot{m}_m V_m}, \quad (A.1)$$

$$T_{ref,I,j} = \frac{\sum_{m \in A_{cr,I,j}} \dot{m}_m T_m}{\sum_{m \in A_{cr,I,j}} \dot{m}_m}, \quad (A.2)$$

The interface reference temperature $T_{ref,I,j}$ is set as the massflow-average temperature for the (free) cross-sectional area $A_{cr,I,j}$ at the interface location. Nusselt numbers for absorber sections and interfaces are calculated as follows, where the air heat conductivity κ_f is evaluated using the corresponding reference temperature:

$$Nu_j = \frac{\dot{q}_j}{T_w - T_{ref,j}} \frac{L_j}{\kappa_f} \quad (A.3)$$

$$Nu_{I,up,j} = \frac{\dot{q}_{I,up,j}}{T_w - T_{ref,I,j}} \frac{L_{abs}}{\kappa_f} \quad (A.4)$$

$$Nu_{I,down,j} = \frac{\dot{q}_{I,down,j}}{T_w - T_{ref,I,j}} \frac{L_{abs}}{\kappa_f} \quad (A.5)$$

By repeating the simulations for different massflow densities and wall temperatures, Nusselt number correlations are derived

with a least-squares fit based on the generic form given in equation A.6.

$$Nu = CRe^{n_1} \left(\frac{T_{ref}}{T_w} \right)^{n_2} \quad (A.6)$$

During the simulations of the 1D model, Nusselt numbers are calculated from the corresponding correlations and then converted to the convective heat transfer coefficients:

$$h_{vol,j} = A_{vol,j} \frac{\kappa_f}{L_j} Nu_j \quad (A.7)$$

$$h_{I,up,j} = \frac{\kappa_f}{L_{abs}} Nu_{I,up,j} \quad (A.8)$$

$$h_{I,down,j} = \frac{\kappa_f}{L_{abs}} Nu_{I,down,j} \quad (A.9)$$

Local temperatures and air properties are used for each evaluation resulting in localized heat transfer coefficients for each mesh element. For the absorber front, Nusselt numbers Nu_{fr} (correlations) and heat transfer coefficients h_{fr} are determined in the same manner as for the interfaces.

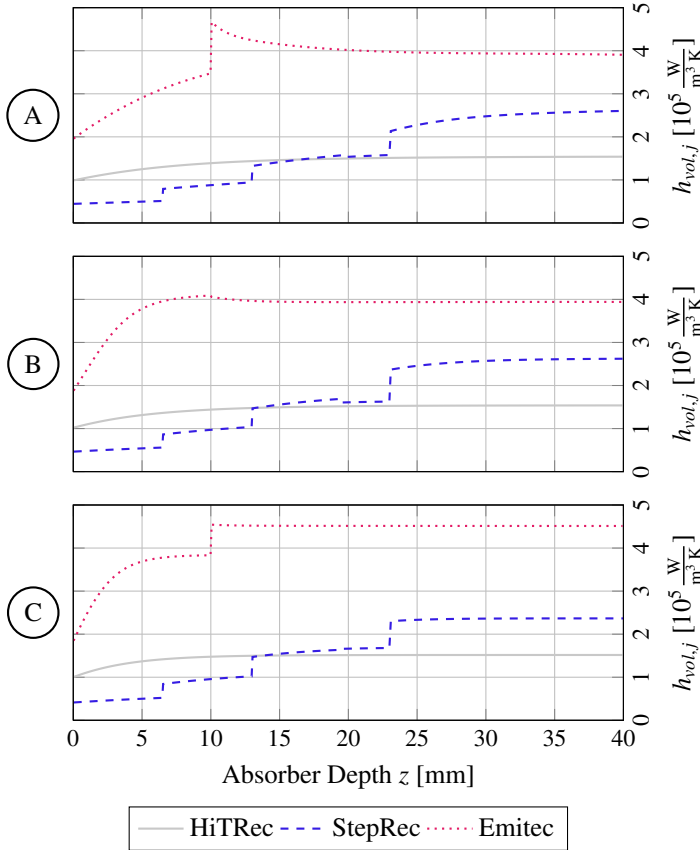


Figure A.1: Volumetric convective heat transfer coefficient over absorber depth for the three absorber geometries and the three simulation cases

In figure A.1 the resulting local values of volumetric convective heat transfer coefficient $h_{vol,j}$ (eq. A.7) are plotted over the absorber depth for the three simulation cases of section 4. Per simulation case, the three absorber geometries are compared against each other. The discontinuities in the StepRec

and Emitec absorbers results correspond to the varying specific surface area values for each absorber section (cf. table 1). Due to having the highest specific surface area, the Emitec absorber also exhibits the highest convective heat transfer coefficient values. Related, the first two sections at the front of the StepRec geometry display the lowest coefficients, but the later sections outperform the HiTRec absorber.

A.3. Pressure Loss Coefficients

The pressure loss within the volumetric absorbers is modeled based on the Darcy-Forchheimer equation (eq. 5). For the continuum model, separate Darcy-Forchheimer coefficients for each absorber section ($d_{df,j}$, $f_{df,j}$), the absorber front ($d_{df,fr}$, $f_{df,fr}$), and each interface ($d_{df,I,j}$, $f_{df,I,j}$) are used. The coefficients are calculated in a two-step process before the main simulations with the 1D-model. For the first part, each section of the respective absorber geometry is simulated individually. These simulations are carried out as three-dimensional, stationary, laminar, and incompressible fluid simulations. The length of the simulated absorber section is increased for these simulations. The added length is used as an inlet area to ensure a fully developed flow within the actual absorber section. The pressure loss is then evaluated for the developed section and the simulations are repeated for different massflow densities. A least-squares fit yields the Darcy-Forchheimer coefficients. The results for the absorber sections of the StepRec geometry are exemplarily shown in figure A.2.

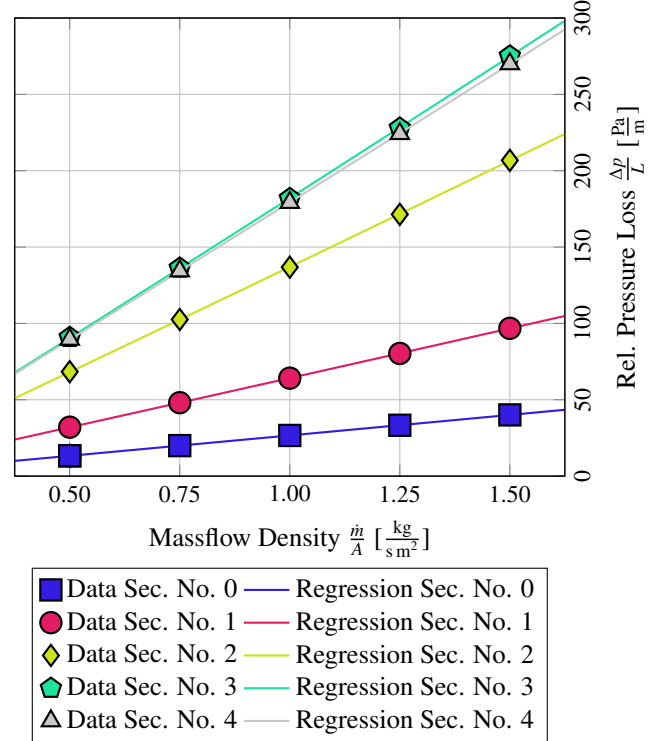


Figure A.2: Relative pressure loss over massflow density for the five absorber sections of the StepRec absorber, massflow density values are defined based on the total cross-section (solid + void)

During the second stage, the pressure loss coefficients for the

interfaces and the absorber front are determined based on the results of the simulations which were conducted to calculate the Nusselt number. For the compressible simulations of the whole absorber unit cell, pressure loss values are evaluated from the middle of each section to the middle of the next downstream section. The interfaces $0 \leq j < N_{sec} - 2$ are then assigned the pressure loss $\Delta p_{I,j}$ which is defined as the difference between the corresponding pressure loss value and the pressure of the two section halves:

$$\Delta p_{I,j} = p_j(0.5) - p_{j+1}(0.5) - 0.5(\Delta p_j + \Delta p_{j+1}), \quad (\text{A.10})$$

With this procedure, the interfaces are assigned the additional pressure loss which is caused by "connecting" two sections compared to the fully-developed flow within the sections. The pressure loss for each section Δp_j is calculated using the Darcy-Forchheimer coefficients which were derived in the first stage. The air density and air viscosity are evaluated based on the reference temperature $T_{ref,j}$ (eq. A.1):

$$\Delta p_j = L_j \left(\mu d_{df,j} + \frac{f_{df,j}}{2} \frac{\dot{m}}{A} \right) \frac{1}{\rho} \frac{\dot{m}}{A} \quad (\text{A.11})$$

The absorber front is given the pressure difference between the ambient pressure p_{in} and the pressure at the middle of the first section, while the last interface ($j = N_{sec} - 2$) receives the pressure difference from the middle of the second last section to the absorber exit:

$$\Delta p_{fr} = p_{in} - p_0(0.5) - 0.5\Delta p_0, \quad (\text{A.12})$$

$$\Delta p_{I,N_{sec}-2} = p_{N_{sec}-2}(0.5) - p_{N_{sec}-1}(1) - 0.5\Delta p_{N_{sec}-2} - \Delta p_{N_{sec}-1}, \quad (\text{A.13})$$

A least-squares fit yields the Darcy-Forchheimer coefficients for the interfaces and the absorber front where the overall absorber length L_{abs} is used as the reference length (cf. eq. 16, eq. 23).

A.4. Absorption Coefficients

The effective parameters for the absorption of the incoming solar radiation consist of the relative, volumetric absorption functions $C_{sol,vol,j}$ (eq. 8) and the interface absorption coefficients $C_{sol,I,j}$ (eq. 20). The absorption functions and coefficients are derived from raytracing simulations of the absorber unit cells. The interface coefficients are derived by dividing the integrated absorbed solar radiation of the corresponding surface by the total incoming radiation. For each absorber section, the calculated absorbed solar radiation of each mesh element is mapped onto the element's position along the main channel axis. The resulting piece-wise constant distribution function is normalized using the incident irradiance and the total absorber length to yield the relative functions $C_{sol,I,j}$.

The relative, volumetric absorption functions $C_{sol,vol,j}$ are plotted over the absorber depth in figure A.3. The functions are identical for simulation cases B and C as the only the aperture irradiance, but not the irradiation direction differs between

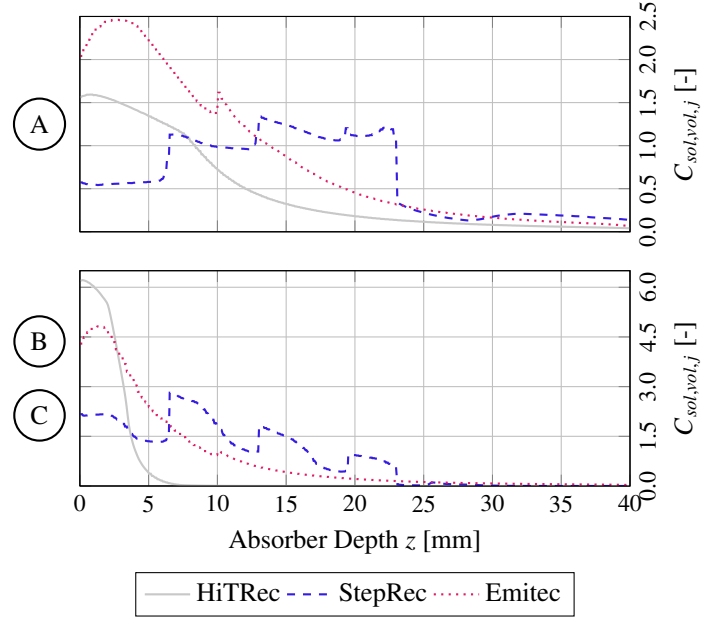


Figure A.3: Relative volumetric absorption functions over absorber depth for the three absorber geometries and the three simulation cases

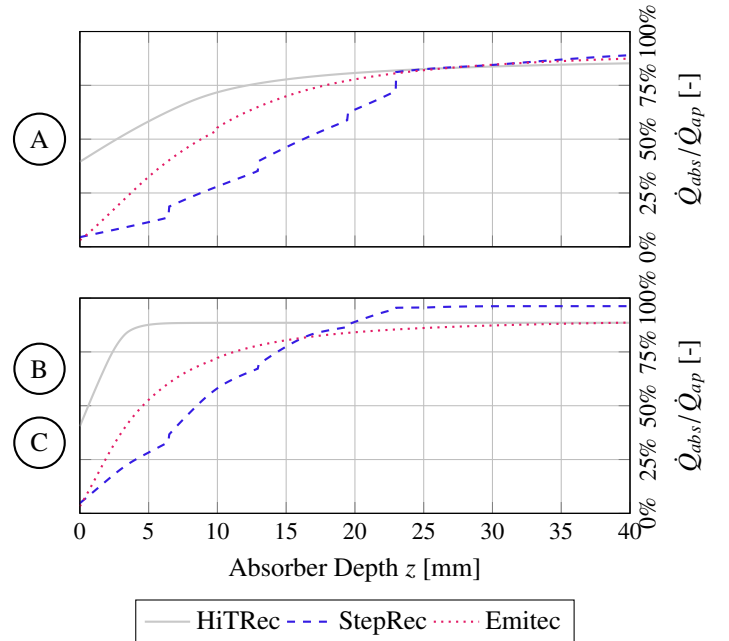


Figure A.4: Accumulated, relative absorbed solar radiation over absorber depth for the three absorber geometries and the three simulation cases

the two cases. The comparison of the three absorber geometries shows that center of the absorption for HiTRec and Emitec is located towards the absorber front, while StepRec allows for a deeper penetration of the solar radiation. The discontinuities between the Emitec and StepRec absorber sections can be related back to the specific surface area (cf. table 1), which is implicitly included in the absorption functions. The inclined ir-

radiation of cases B and C compared to case A moves the center of the absorption to the front for all absorbers. In order to also visualize the effect of the interface absorption coefficients $C_{sol,I,j}$, the accumulated absorbed solar radiation \dot{Q}_{abs} as a function of the absorber depth is shown in figure A.4 relative to the incoming radiation \dot{Q}_{ap} (eq. 26). Each interface absorption coefficient corresponds to a jump in the absorbed solar radiation, best visible for the StepRec geometry, while the initial values are defined by the power absorbed at the absorber front (eq. 24).

A.5. Viewfactors

The model for the thermal radiation introduced in section 3.3 requires effective viewfactors between the volume, inlet and outlet, interface, and mirror elements. First, viewfactors are determined numerically for 3D surface meshes of the absorber geometries, from which the effective viewfactors are derived. The simple HiTRec geometry has no openings in the channel walls, no thermal radiation is exchanged between neighboring absorber channels. Thus, the viewfactors can be directly evaluated and the radiation model can be simplified accordingly ($N_{uc} = 1, N_{mir} = 0$). To calculate the viewfactors, the channel walls of a 3D surface mesh are divided along the main channel axis as shown in figure A.5.

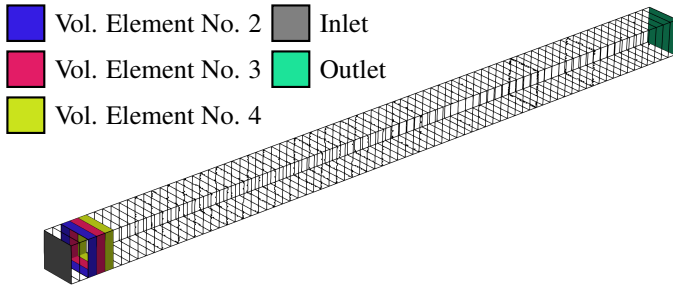


Figure A.5: Division of the absorber walls for the viewfactor calculation for the HiTRec absorber. Highlighted are the wall segments of the second, third and fourth volume element, and the inlet and the outlet element.

Each of the $N_{el,vol}$ volume elements is assigned one segment of each of the four channel walls for the HiTRec absorber. Subsequently, the mesh elements of the 3D mesh are grouped into sets $E(k)$ that make up each element k of the volume, inlet, and outlet elements. E.g. for each volume element, the created set consists of the mesh elements of the corresponding four channel wall segments. The numerical tool, which is part of OpenFOAM®(2021), calculates the viewfactors $\Psi_{n,m}$ between two mesh elements n and m . The effective viewfactors $\Psi_{k,l}^{eff}$ needed by the continuum model between radiation elements k and l are then defined as:

$$\Psi_{k,l}^{eff} = \frac{1}{A_k} \sum_{n \in E(k)} A_n \sum_{m \in E(l)} \Psi_{n,m} \quad (\text{A.14})$$

Radiation exchange between neighboring absorber channels is possible for the StepRec and Emitec absorber due to partial openings in the channel walls. As identical temperature profiles

are assumed for the neighboring channels, the radiation model would ideally use viewfactors for a perfectly periodic absorber structure. However, this is not possible with the given viewfactor calculation tool. Instead, unit cell patterns as demonstrated in figure A.6 are used. The openings in the outer channel walls of the outermost unit cells are replaced by perfectly reflecting side elements. The viewfactors are then calculated for the closed unit cell pattern. The absorber walls of each unit cell (original + clones) are divided into volume elements in the same manner as for the HiTRec absorber. Therefore, the calculation yields effective viewfactors between the volume elements of each absorber channel, the inlet and outlet elements, and the side elements.

During the evaluation of the radiation model (cf. sec. 3.3), the

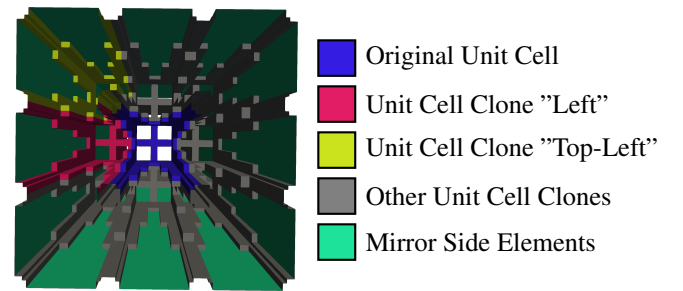


Figure A.6: Unit pattern for viewfactor calculation for the StepRec absorber. The "left" and "top-left" unit cell clone are highlighted exemplarily. Not shown are the inlet and outlet elements.

1D temperature profile of the solid phase is applied as the temperature distribution of each unit cell. For the exemplary unit cell pattern shown in figure A.6, it would be assumed that all nine absorber channels have the same temperature distribution. The radiative exchange for the whole unit cell pattern including the side elements is then calculated, but only the net radiative flux for the original unit cell is used to calculate the source term for the temperature equation (eq. 13). The idea behind this approach is that the interaction (i.e. viewfactors) between the original unit cell and the artificial side elements, which are necessary for the closure of the radiative energy balance, decrease by adding the unit cell clones. With an increasing size of the used unit cell pattern, the solution of the radiation exchange is expected to converge towards the solution with periodic viewfactors. However, the numerical effort scales quadratically with the number of mesh elements, which is proportional to the number of unit cells. As a compromise, three-by-three unit cell patterns have been used for the StepRec and Emitec absorber geometries.